The Impact of a Partially Molten YSZ Particle

Tommy Che-Ming Wu, Markus Bussmann, and Javad Mostaghimi

In plasma and high velocity oxy-fuel spraying, a certain portion of the injected powder is often not fully molten upon impact onto a substrate. We present numerical results of the impact of a partially molten yttria-stabilized zirconia particle, a material widely used as a thermal barrier. We consider an idealized scenario: the axisymmetric impact of a particle with a solid core, examining only the flow of the molten material around the core. The numerical method is based on the immersed boundary method for treating the interaction of solids and fluid within a computational domain. We present the results of a set of simulations, varying the particle and solid core diameters, and the impact velocity. When the core diameter is small relative to the particle, the impact behavior is similar to the impact of a fully molten droplet. When the core is larger, it promotes considerable splashing, which is undesirable.

1. Introduction

Thermal-sprayed coatings are widely used for diverse applications including, for example, to protect substrates from corrosion, wear, and high temperature; to enhance the biocompatability of implants; and to fabricate solid oxide fuel cells (Ref 1). In general, material in powder form is injected into a heat source (e.g., a plasma or combustion jet); the particles are entrained by the jet, accelerate and melt, and upon impact onto a substrate, spread and solidify into lamellar splats. A coating is the agglomeration of many such splats, piled one on top of another.

A common characteristic of thermal-sprayed coatings is the presence of a small fraction of particles that were not entirely molten upon impact. Figure 1 is a micrograph of a cross section of a yttria-stabilized zirconia (YSZ) coating produced by atmospheric plasma spraying (SG-100 torch, Praxair). In the middle of the figure are several particles that impacted as solid, evidenced by the fact that close inspection reveals that the particle microstructure is equiaxed, which is characteristic of YSZ powder, in contrast with the columnar microstructure visible elsewhere in the cross section, that forms during the rapid solidification of molten YSZ; this also suggests that the particles are not simply fragments of a molten particle that splashed on impact. Also, note that the particles are not spherical,

perhaps because they deformed on impact and/or because YSZ is not a pure material.

There are several reasons why a small fraction of particles will not completely melt (Ref 2, 3): some particles are simply too large to be completely melted during the residence time associated with a typical trajectory through the jet; some trajectories are far enough off the jet centerline that the particles will not encounter the temperatures necessary for complete melting; and in some cases the jet itself may not be hot enough to guarantee melting of all particles, because excessive temperature will exacerbate particle oxidation (of metals) and vaporization.

The presence of solid particles in a coating is usually associated with increased porosity; presumably the solid particle on impact protrudes from the coating surface, disrupting the smooth spread of subsequent molten particles, and so voids form beneath and around the solid particle. Experimental evidence of porosity in the vicinity of solid particles has been corroborated by analytical (Ref 4) and numerical (Ref 5) models of the impact of a single particle; such behavior is also an assumption of stochastic models that predict coating properties (Ref 6).

What is not clear, however, is how the molten fraction of a partially molten particle spreads, how the solid core affects that flow, and more generally how the impact of a partially molten particle compares with that of a fully molten one. Molten particle impact has been modeled for most of 20 years, beginning with relatively simple models of the axisymmetric impact of a particle onto a flat surface (e.g., Ref 7); more recent models are fully 3D and account for both flow and solidification (e.g., Ref 8), which allows for the prediction of more complex behavior such as splashing.

In this paper, we present results of a study of the impact of a partially molten YSZ particle, to begin to answer some of the aforementioned questions. We consider a very idealized scenario: the axisymmetric impact of a particle with a solid spherical core, examining only the flow of molten material around a core that is already at rest on the substrate, as illustrated in Fig. 2. In what follows we present details of the numerical model, and

Tommy Che-Ming Wu, Markus Bussmann, and **Javad Mostaghimi**, Centre for Advanced Coatings Technology, University of Toronto, Toronto, ON, Canada; and Department of Mechanical and Industrial Engineering, University of Toronto, 5 King's College Road, Toronto, ON M5S 3G8, Canada. Contact e-mail: mostag@mie.utoronto.ca.
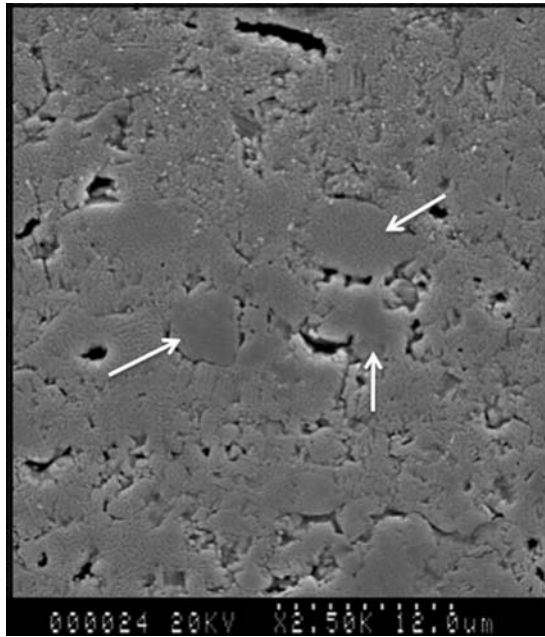
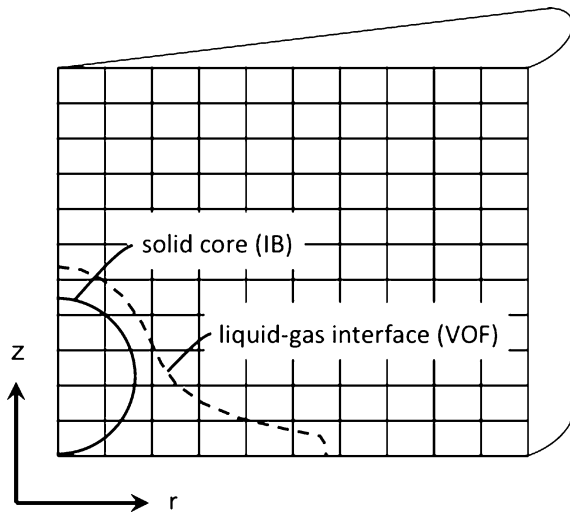**Fig. 1** Micrograph of the cross section of a YSZ splat

Fig. 2 The solid core is modeled via the IB method; the liquid-gas interface via the VOF method

then the results of a set of simulations, systematically varying the particle and solid core diameters, and the impact velocity.

2. Methodology

In this section, the mathematical model is presented, followed by an overview of the immersed boundary (IB) method for imposing the no-slip condition along the solid

core, and finally the overall solution methodology is presented. The use of an IB method in a model of thermal spray splat formation is uncommon. IB methods (for an overview, see Ref. 9) provide a means of introducing complex solid geometries into Eulerian flow calculations, including the movement of solid material through the flow. As applications of splat flow and phase change simulations continue to increase in complexity, IB methods represent an attractive approach to treating solid/fluid interactions.

2.1 Equations

The impact of a partially molten YSZ particle is idealized as axisymmetric, and the fluids (both the molten YSZ and the surrounding gas) are assumed incompressible and Newtonian. The governing flow equations are then expressions of conservation of mass (equivalent to volume) and momentum:

$$\nabla \cdot u = 0 \tag{Eq 1}$$

$$\frac{\partial(\rho u)}{\partial t} + \nabla \cdot (\rho u \otimes u) = -\nabla p + \nabla \cdot \tau + \rho g + F_{ST} + F_{IB} \tag{Eq 2}$$

u is the velocity vector, ρ is density, t is time, p is pressure, g is the gravity vector, F_{ST} is the surface tension force, F_{IB} is the IB force, and $\tau = \mu(\nabla u + \nabla^T u)$ is the viscous stress tensor, where μ is the fluid viscosity.

A scalar field f is used to track the liquid-gas interface: $f = 1$ indicates, say, the liquid, and $f = 0$ the gas, and this field is advected with the flow:

$$\frac{\partial f}{\partial t} + \nabla \cdot (uf) = 0 \tag{Eq 3}$$

The liquid-gas surface tension force F_{ST} is evaluated as a body force via the continuum surface force (CSF) model of Brackbill et al. (Ref 10). The IB force F_{IB} is a numerical construct used to enforce the no-slip condition at solid-fluid boundaries internal to the computational domain (here, at the surface of the fixed solid core); F_{IB} is evaluated via the direct forcing model of Uhlmann (Ref 11).

2.2 Numerical Model

Figure 2 illustrates the grid geometry. The flow code is based on that of Lucente (Ref 12): the flow model is a collocated finite volume scheme (velocities are calculated at both cell centers and faces; pressure and the scalar f are only calculated at cell centers); the liquid-gas interface is tracked via a volume-of-fluid (VOF) method. The solid core within the YSZ particle is treated as an IB via the method of Uhlmann (Ref 11)—note that we did not implement Uhlmann's flow solver); this particular variant of an IB method was chosen because Kuipers and coworkers (Ref 13) have incorporated this method into a VOF code not dissimilar to ours, to study fluidized beds. The method of Uhlmann allows for solid material to move through a flow; in the work presented here, since

we assume the solid core to be at rest on the substrate, we have implemented a simplified version of the Uhlmann model.

The IB is defined by a set of massless points that need not coincide with the gridpoints of the Eulerian fixed mesh (the IB points are said to represent a Lagrangian mesh). As illustrated in Fig. 3, the force points were distributed evenly (every $\Delta\theta$) on the semi-circle that defines the surface of the solid core. Figure 3 also illustrates that the points are associated with their own control volumes that should be of comparable size to the Eulerian control volumes (Ref 11). Referring again to Fig. 3, r_o and r_i refer to the outer and inner radii of the IB control volumes; we set $r_o - r_i \approx h$, the Eulerian mesh spacing, and then calculated $\Delta\theta$. (Fig. 4).

Equations 1-3 are solved repeatedly for discrete values of u, p, and f at time increments $\Delta t = t^{n+1} - t^n$. At each timestep, the f field is advected first by solving Eq 3, which
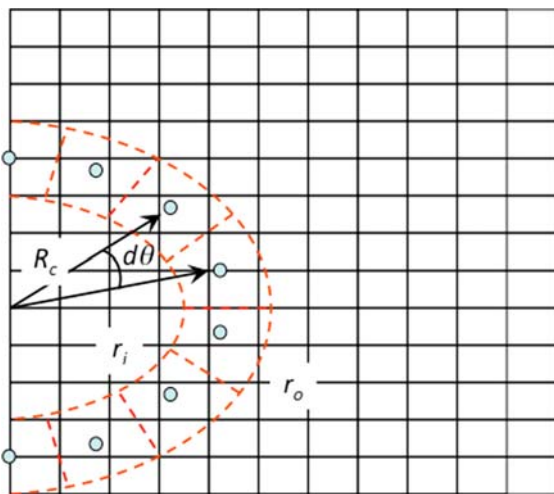

Fig. 3 The IB force points and the associated control volumes distributed on the Eulerian mesh

yields a time $n + 1$ liquid-gas interface position; Eq 1 and 2 are then solved for velocities and pressure.

The scalar function f is discretized by integrating over each control volume; the resulting volume fractions f_{ij} reflect whether a cell is entirely filled with liquid or gas, or contains a portion of the liquid-gas interface ($0 < f_{ij} < 1$, referred to as interface cells). At each timestep, Eq 3 is solved geometrically: the liquid-gas interface is reconstructed (in the interface cells) as piecewise linear segments (this is commonly referred to as a PLIC method), with normals calculated via the ELVIRA method of Pilliod and Puckett (Ref 14). The volume fractions are then advected via the method of Youngs (Ref 15), which discretizes Eq 3 by operator splitting, and so advects the volume fractions one dimension at a time, alternating the order of advection from one timestep to the next to minimize any directional bias. Finally, the new volume fractions are used to calculate an updated density field:

$$\rho_{ij}^{n+1} = f_{ij}^{n+1}\rho_{liq} + \left(1 - f_{ij}^{n+1}\right)\rho_{gas}.$$

The momentum equation is then solved via a multistep projection method; the following three equations when summed are a time discretization of Eq 2:

$$\frac{(\rho^{n+1}u^*) - (\rho u)^n}{\Delta t} = -\nabla \cdot (\rho uu)^n - \nabla p^n + \nabla \cdot \tau^n + F_{ST}^n \tag{Eq 4}$$

$$\frac{(\rho^{n+1}u^{**}) - (\rho^{n+1}u^*)}{\Delta t} = \nabla p^n + F_{IB}^* \tag{Eq 5}$$

$$\frac{(\rho^{n+1}u^{n+1}) - (\rho^{n+1}u^{**})}{\Delta t} = -\nabla p^{n+1} \tag{Eq 6}$$

where u^* and u^{**} are interim velocities calculated during the timestep.

In step 1, Eq 4, u^* is a first estimate of the velocities at the next timestep, based on contributions from the convective, pressure, viscous, and surface tension terms calculated explicitly from time n values of velocity and pressure, without regard for enforcing either the
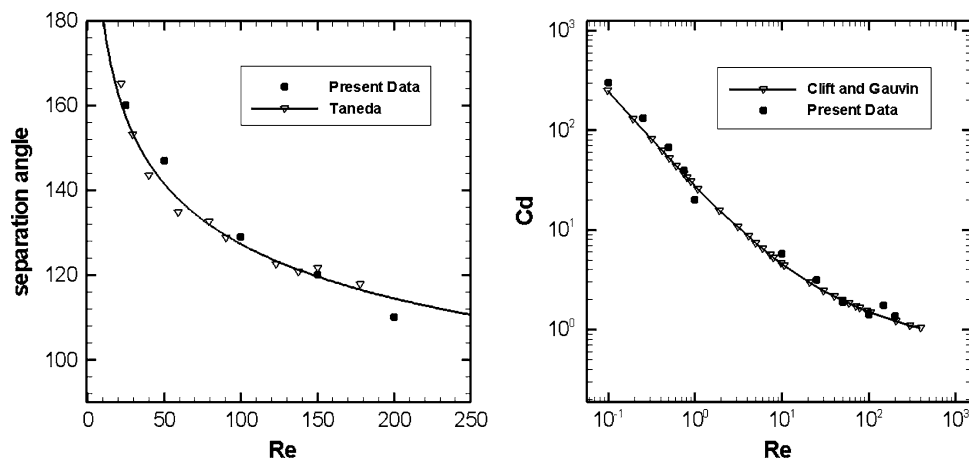

Fig. 4 Validation results: separation angle (*left*) and drag coefficient (*right*) vs. *Re* for axisymmetric flow past a sphere

continuity constraint (Eq 1) or the no-slip condition at immersed boundaries. The mass flux components of the convective term are calculated in a manner consistent with the volume fluxes calculated during the volume tracking step, as per Ref 16; the convected velocities are calculated via the method of van Leer (Ref 17) except near the liquid-gas interface, where simple upwind values are used. The viscous and pressure terms are discretized with standard central differences. Finally, the surface tension term is calculated simply as $F_{ST} = \sigma\kappa\nabla f$ (where σ is the surface tension coefficient and κ is the interface curvature), which is the so-called balanced-force approach recommended by Francois et al. (Ref 18).

At this point, the Eulerian values of u^* are interpolated to each of the IB points on the Lagrangian mesh; for the mth IB point located within the Eulerian cell (i, j):

$$u_m^* = \sum_{k,n=-1}^{1} u_{i+k,j+n}^* \delta(x_{i+k,j+n} - x_m)\Delta V_{i+k,j+n} \qquad \text{(Eq 7)}$$

where x_m is the vector to the mth IB point, the $x_{i+k,j+n}$ and $\Delta V_{i+k,j+n}$ are position vectors to, and volumes of, the neighboring Eulerian cell centers, and δ is the kernel (or convolution function) that defines the interpolation weighting of velocities from the 3×3 stencil; we implemented the discrete δ of Roma et al. (Ref 19).

Values of F_{IB} can now be calculated; these are the forces necessary to impose the no-slip velocity at each Lagrangian IB point:

$$F_{IB,m} = -\frac{\rho u_m^*}{\Delta t} \qquad \text{(Eq 8)}$$

Finally, these forces are transferred back onto the Eulerian grid in a reverse of the interpolation embodied by Eq 7:

$$F_{IB}(i,j) = \sum_{m=1}^{nb} F_{IB,m}(x_m)\delta(x_m - x_{i,j})\Delta V_m \qquad \text{(Eq 9)}$$

where nb is the number of IB points and ΔV_m is the volume of the mth IB control volume.

Returning to Eq 4-6, the second step (Eq 5) of the method yields the second interim velocity u^{**}, by adding the F_{IB} to enforce the no-slip condition at the immersed boundaries, but removing the time n pressure gradient that was added in the first step.

The final step is the evaluation of u^{n+1}. Taking the divergence of Eq 6, and combining this with Eq 1 yields the following Poisson equation for p^{n+1} that enforces the continuity equation:

$$\nabla \cdot \frac{\nabla p^{n+1}}{\rho^{n+1}} = -\frac{\nabla \cdot u^{**}}{\Delta t} \qquad \text{(Eq 10)}$$

Finally, Eq 6 yields the divergence-free u^{n+1}.

3. Results and Discussion

The flow model plus IB implementation was tested in various ways to assess the accuracy of results. Figure 4 illustrates the results of one set of those tests, of uniform flow past a solid sphere at different Reynolds numbers, Re. These simulations were run on meshes of 80×240 cells at low Re, and 25×125 cells at higher Re (when the flow separates); results obtained on other meshes confirmed that these results were nearly mesh independent. The left plot compares values of the flow separation angle to the experimental results of Taneda (Ref 20); the right plot compares values of the drag coefficient to the correlation of Clift and Gauvin (Ref 21). Note that at low Re the flow does not separate, and so we present only the drag coefficient. The agreement over a wide range of Re is good, and no worse than the usual agreement between simulation and experiment for these types of measurements.

Turning to the impact of a partially molten YSZ particle, we ran a set of simulations at a resolution of 50 cells per particle diameter, on a domain of $2.0\ D_o \times 1.25\ D_o$, systematically varying the initial particle size D_o, solid core size D_c, and impact velocity V; a summary of the simulations is presented in Table 1 (note that case 1 is of a fully molten particle). The effect of further increases in domain size was determined to be negligible, as the gas phase has a very small effect on the dynamics of the impacting particle. We also ran test simulations at higher resolutions (cells per diameter): the macroscopic results varied little from those presented here, although fine scale phenomena (such as will be presented in Fig. 6) varied somewhat at each resolution we tested. The following YSZ fluid properties were specified: density $\rho = 5560$ kg/m^3; dynamic viscosity $\mu = 0.029$ kg/ms; and surface tension $\sigma = 0.43$ N/m; the surrounding gas phase was assumed inviscid with a density of 1 kg/m^3. The contact angle (at the advancing contact line) was specified as 90°, for lack of a better value. Finally, to simplify the simulations, both the solid core and the surrounding fluid were initialized at positions immediately above the substrate, as illustrated in the first of the snapshots presented in both Fig. 5 and 6. The fluid was assigned the initial impact velocity; the surrounding gas phase was assumed initially quiescent; the position of the solid core was fixed throughout the impact.

Figures 5 and 6 illustrate two impacts that are representative of all the results we obtained. Figure 5 corresponds to case 5 (Table 1), the 100 m/s impact of a 50 μm particle with a 20 μm solid core; similar results were obtained for cases 2, 4, and 6. The results are similar to what one would see of the impact of a fully molten particle. Immediately upon impact a thin axisymmetric sheet of fluid accelerates rapidly outward (see $t^* \equiv tV/D_o = 0.34$); as the expansion of the leading edge of the sheet slows, the sheet becomes thicker ($t^* = 0.89$); eventually the leading edge of the sheet reaches some maximum diameter, and then under the action of surface tension and the contact angle at the leading edge, a rim of fluid forms at the periphery and the edge of the sheet retracts (in this case) slowly ($t^* = 2.56$ and $t^* = 13.37$). There are only two noticeable differences between this and the impact of a fully molten particle: (i) obviously the core remains at the center of the splat, and (ii) a bump appears in the fluid profile next to the core, visible at $t^* = 1.57$. Figure 7
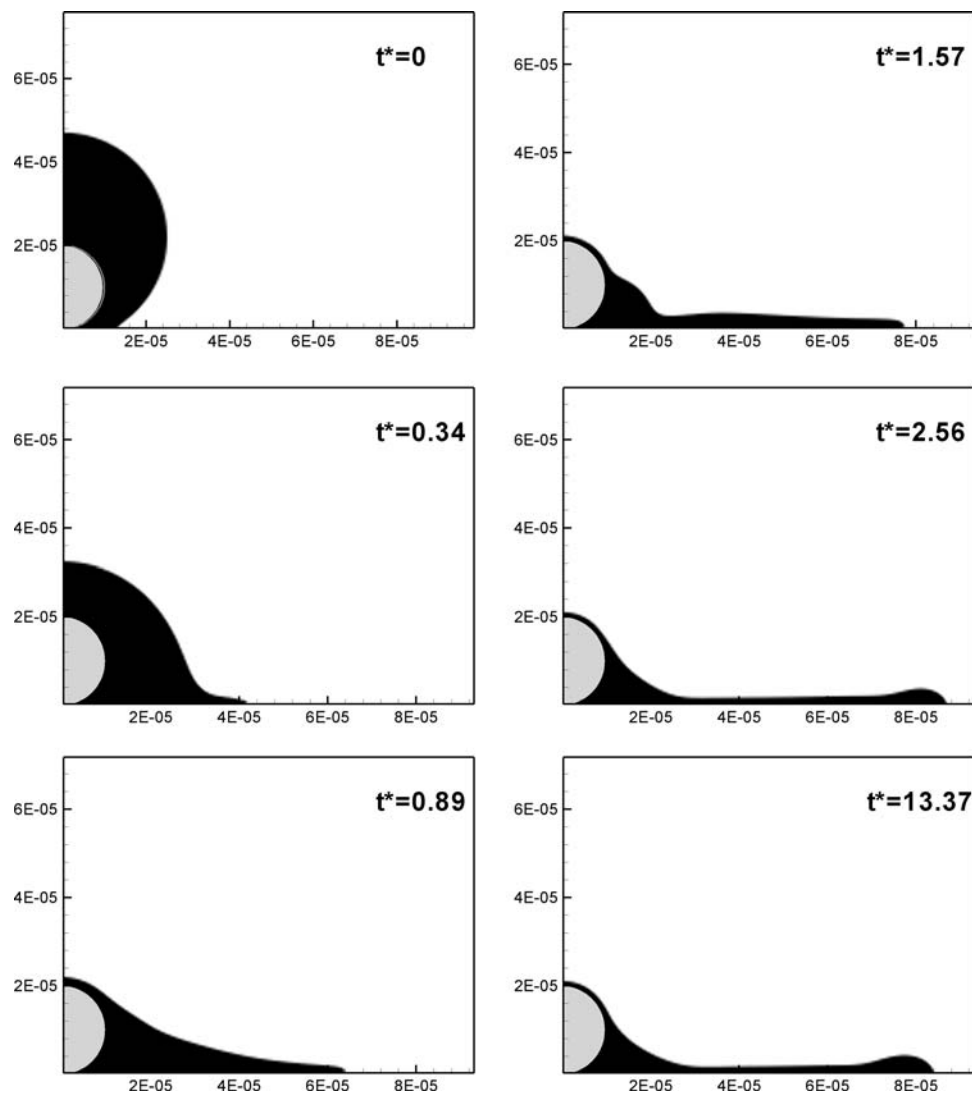
Fig. 5 Snapshots of the impact of a 50 μm particle with a 20 μm core impacting at 100 m/s

Table 1 A summary of the simulations

	Overall particle diameter, μm	Solid core diameter, μm	Impact velocity, m/s
1	100	0	100
2		20	
3		40	
4	50	10	
5		20	
6		30	
7	100	50	100
8			200
9			250

illustrates fluid streamlines within this region at $t^* = 0.89$ and 1.57, and clearly shows a recirculation region that becomes more prominent as the fluid layer above the region thins. Such a vortical flow is not seen in impacts of fully molten particles, but as Fig. 5 illustrates, the recirculation in this case (and in cases 2, 4, and 6) dies out at

later times and does not dramatically affect the final splat shape.

The effect of the recirculation zone is much more dramatic in cases 3, 7, 8, and 9. Figures 6 and 8 illustrate case 8, the 200 m/s impact of a 100 μm particle with a 50 μm solid core. In this case, the effect of the recirculation zone is more dramatic, perhaps because the core is relatively larger and/or because the velocity is higher than for case 5 (Fig. 5). The recirculation zone at $t^* = 0.53$ is relatively small, but by $t^* = 1.34$, when little fluid remains above the core, the vortex, spinning clockwise in the figure, has generated a significant distortion of the free surface of the liquid layer. Returning to Fig. 6, the final three frames, beginning at $t^* = 2.38$, illustrate that the vortex leads to the ejection of a fluid sheet up and outward from the core, a sheet that eventually breaks up into small droplets.

As noted, this behavior, of a vortex entraining fluid and then ejecting it upwards, was predicted for several
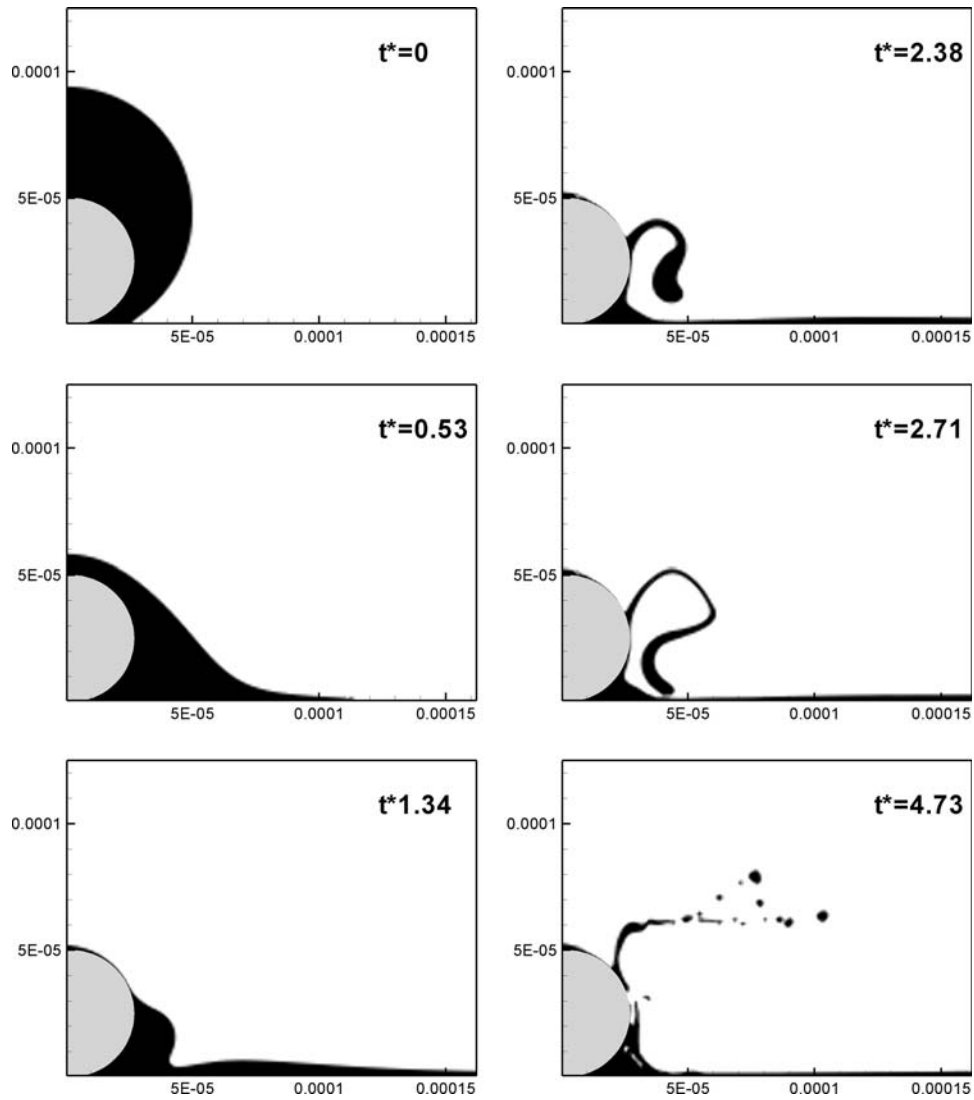
Fig. 6 Snapshots of the impact of a 100 μm particle with a 50 μm core impacting at 200 m/s
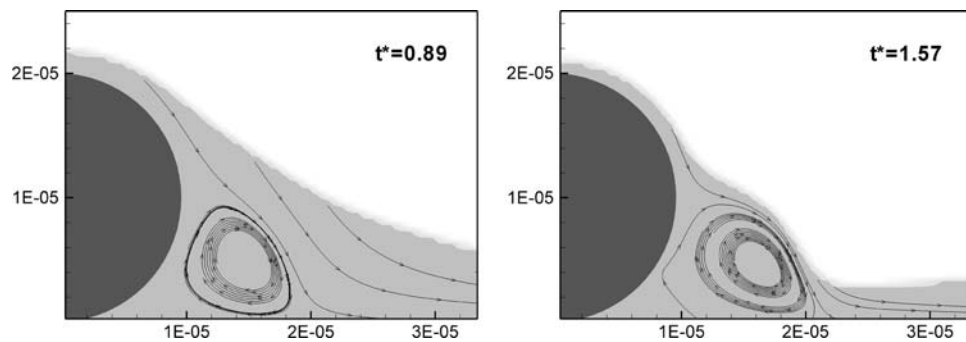

Fig. 7 The recirculation zone, for the impact of a 50 μm particle with a 20 μm core impacting at 100 m/s

cases, generally those characterized by a larger core and a higher impact velocity. The details of the ejection behavior varied from one case to another, and we would not suggest that these particulars, given the assumptions behind the model, are quantitatively accurate. On the other hand, the simulations strongly suggest that the presence of a core can lead to flow features that have the potential to disrupt what would otherwise be a
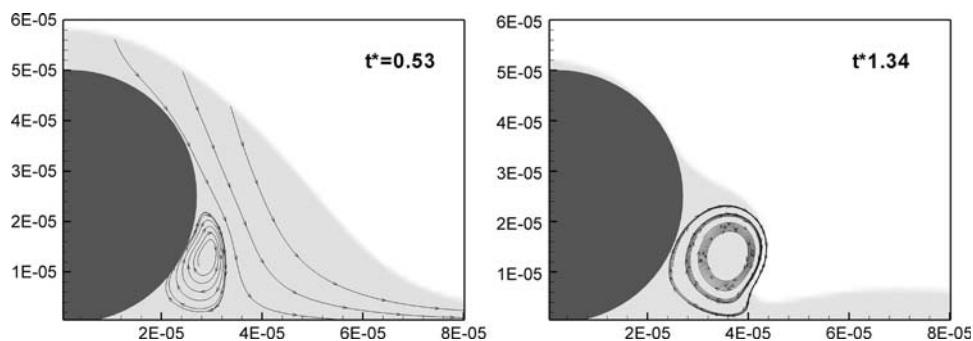
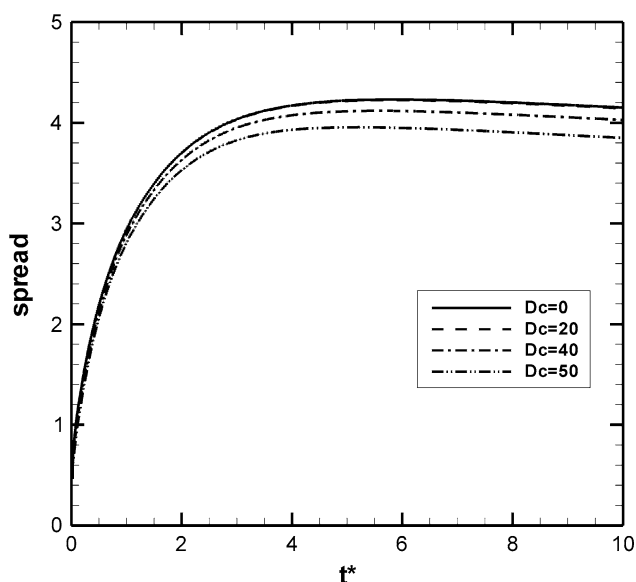**Fig. 8** The recirculation zone, for the impact of a 100 μm particle with a 50 μm core impacting at 200 m/s

Fig. 9 Spread factor vs. t^* for a 100 μm particle impacting at 100 m/s, as a function of solid core diameter D_c (μm)
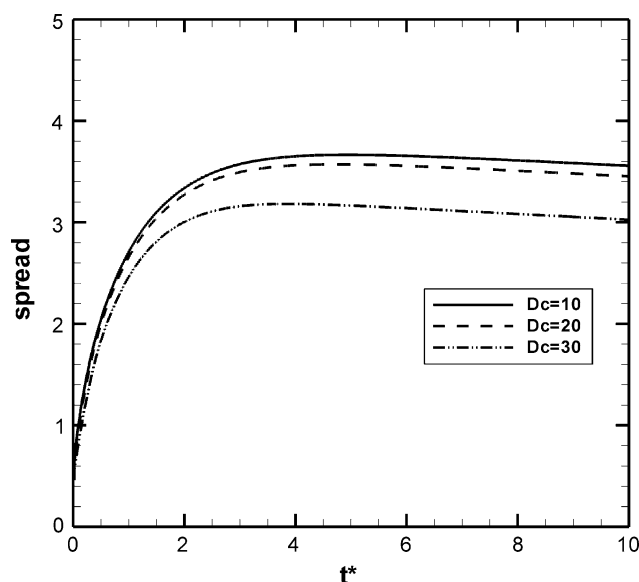

Fig. 10 Spread factor vs. t^* for a 50 μm particle impacting at 100 m/s, as a function of solid core diameter D_c (μm)

smooth deposition of fluid onto a substrate or onto previously deposited splats.

Finally, Fig. 9 to 11 illustrate curves of spread factor (defined as D/D_o, where D is the instantaneous diameter of the splat) versus nondimensional time. Figure 9 illustrates the spread of 100 μm particles with different sized cores, impacting at 100 m/s, compared to the spread of a fully molten particle. Note that the particles spread rapidly at very similar rates early on, and by $t^* \approx 3$ have reached their maximum spread. The effect of the 20 μm core is negligible; the 40 and 50 μm cores reduce the spread somewhat. The primary reason for the relatively small variations in spread is that the fluid fraction of a particle varies as $1 - (D_c/D_o)^3$, which means that the 20, 40, and 50 μm cores still leave fluid fractions of 0.99, 0.94, and 0.88—in other words, these particles are mostly molten. Figure 10 makes the same point for 50 μm particles; this time the spread is somewhat less for the particle with the 30 μm core, which leaves a fluid fraction of 0.78. Finally, Fig. 11 illustrates the variation of spread of a 100 μm

particle with a 50 μm core (corresponding to a fluid fraction of 0.88) as a function of velocity. As would be the case for fully molten particles, fluid spreads further at higher velocities.

4. Conclusions

In this paper, we presented a model for the impact of partially molten particles. The model employs the IB method to accurately capture the interaction of the flow with the solid core. Presently, the model does not consider heat transfer effects and assumes such effects are negligible on the flow field. This is a reasonable assumption considering that solidification time is typically one order of magnitude larger than the spreading time of molten droplets impacting a surface. The model has been applied to the impact of a YSZ particle impacting the substrate at a normal angle. Two particles sizes (50 and 100 μm) were
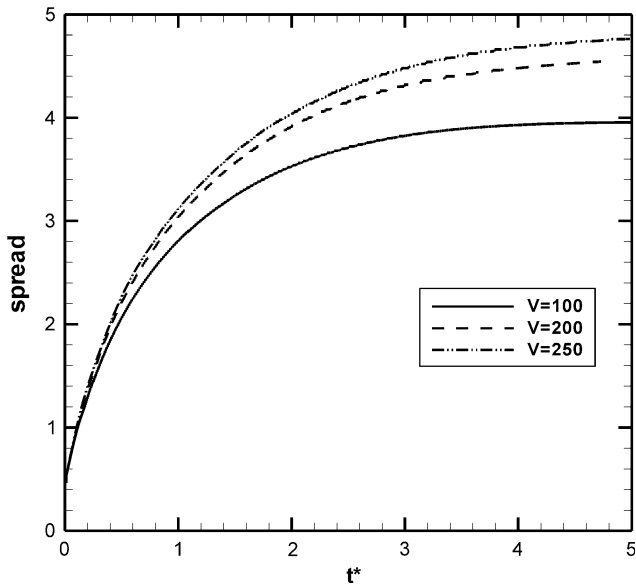
Fig. 11 Spread factor vs. t^* for a 100 μm particle with a 50 μm core, as a function of impact velocity V (m/s)

considered. The solid core size of the particle was varied. We demonstrated that, compared to the particle diameter, when the solid core is small, the impact is similar to the impact of a fully molten droplet. However, as the solid core becomes bigger, splashing occurs. Splashing is undesirable and should be avoided. In the future, we will extend the model to include heat transfer and phase change.

References

1. L. Pawlowski, *The Science and Engineering of Thermal Spray Coatings*, 2nd ed., Wiley, Chichester, England, 2008
2. M. Friis, C. Persson, and J. Wigren, Influence of Particle In-Flight Characteristics on the Microstructure of Atmospheric Plasma Sprayed Yttria Stabilized ZrO_2, *Surf. Coat. Tech.*, 2001, **141**(2-3), p 115-127
3. J. He, M. Ice, and E. Lavernia, Particle Melting Behavior During High-Velocity Oxygen Fuel Thermal Spraying, *J. Therm. Spray Technol.*, 2001, **10**(1), p 83-93
4. H. Liu, E.J. Lavernia, and R.H. Rangel, Modeling of Molten Drop Impingement on a Non-flat Surface, *Acta Metall. Mater.*, 1995, **43**(5), p 2053-2072
5. H. Fukanuma, Porosity Formation and Flattening Model of an Impinging Molten Particle in Thermal Spray Coatings, *J. Therm. Spray Technol.*, 1994, **3**(1), p 33-44
6. M. Xue, S. Chandra, J. Mostaghimi, and C. Moreau, A Stochastic Coating Model to Predict the Microstructure of Plasma Sprayed Zirconia Coatings, *Model. Simul. Mater. Sci. Eng.*, 2008, **16**(6), 065006 (19 p)
7. G. Trapaga and J. Szekely, Mathematical Modeling of the Isothermal Impingement of Liquid Droplets in Spraying Processes, *Metall. Trans. B*, 1991, **22**(6), p 901-914
8. H.B. Parizi, L. Rosenzweig, J. Mostaghimi, S. Chandra, T. Coyle, H. Salimi, L. Pershin, A. McDonald, and C. Moreau, Numerical Simulation of Droplet Impact on Patterned Surfaces, *J. Therm. Spray Technol.*, 2007, **16**(5-6), p 713-721
9. R. Mittal and G. Iaccarino, Immersed Boundary Methods, *Annu. Rev. Fluid Mech.*, 2005, **37**, p 239-261
10. J.U. Brackbill, D.B. Kothe, and C. Zemach, A Continuum Method for Modeling Surface Tension, *J. Comput. Phys.*, 1992, **100**(2), p 335-354
11. M. Uhlmann, An Immersed Boundary Method with Direct Forcing for the Simulation of Particulate Flows, *J. Comput. Phys.*, 2005, **209**(2), p 448-476
12. M. Lucente, "A Numerical Study of Axisymmetric Droplet Impact of a Shear Thinning Fluid," M.A.Sc. thesis, Unversity of Toronto, 2006
13. M.A. van der Hoef, M. van Sint Annaland, N.G. Deen, and J.A.M. Kuipers, Numerical Simulation of Dense Gas-Solid Fluidized Beds: A Multiscale Modeling Strategy, *Annu. Rev. Fluid Mech.*, 2008, **40**, p 47-70
14. J.E. Pilliod and E.G. Puckett, Second-Order Accurate Volume-of-Fluid Algorithms for Tracking Material Interfaces, *J. Comput. Phys.*, 2004, **199**(2), p 465-502
15. D.L. Youngs, Time-Dependent Multi-Material Flow with Large Fluid Distortion, *Numerical Methods for Fluid Dynamics*, K.W. Morton and M.J. Baines, Eds., Academic Press, New York, 1982, p 273-285
16. M. Bussmann, D.B. Kothe, and J.M. Sicilian, Modeling High Density Ratio Incompressible Interfacial Flows, FEDSM2002-31125, *Proceedings of the 2002 ASME Joint U.S.-European Fluids Engineering Conference*, Montreal, 2002
17. B. van Leer, Towards the Ultimate Conservative Difference Scheme. V. A Second-Order Sequel to Godunov's Method, *J. Comput. Phys.*, 1979, **32**(1), p 101-136
18. M. Francois, S.J. Cummins, E.D. Dendy, D.B. Kothe, J.M. Sicilian, and M.W. Williams, A Balanced-Force Algorithm for Continuous and Sharp Interfacial Surface Tension Models Within a Volume Tracking Framework, *J. Comput. Phys.*, 2006, **213**(1), p 141-173
19. A.M. Roma, C.S. Peskin, and M.J. Berger, An Adaptive Version of the Immersed Boundary Method, *J. Comput. Phys.*, 1999, **153**(2), p 509-534
20. S. Taneda, Experimental Investigation of the Wake Behind a Sphere at Low Reynolds Numbers, *J. Phys. Soc. Jpn*, 1956, **11**, p 1104-1108
21. R. Clift, J.R. Grace, and M.E. Weber, *Bubbles, Drops, and Particles*, Academic Press, San Diego, 1978